Nano Research
2021, 14(5): 1541–1550

ISSN 1998-0124 CN 11-5974/O4
https://doi.org/10.1007/s12274-020-3213-y

Research Article

# A dual-functional poly(vinyl alcohol)/poly(lithium acrylate) composite nanofiber separator for ionic shielding of polysulfides enables high-rate and ultra-stable Li-S batteries

Chunyang Zhou[1], Jing Wang[4], Xiaobo Zhu[1], Kai Chen[1], Yue Ouyang[1], Yue Wu[3], Yue-E Miao[1] (✉), and Tianxi Liu[1,2]

[1] *State Key Laboratory for Modification of Chemical Fibers and Polymer Materials, College of Materials Science and Engineering, Innovation Center for Textile Science and Technology, Donghua University, 2999 North Renmin Road, Shanghai 201620, China*
[2] *Key Laboratory of Synthetic and Biological Colloids, Ministry of Education, School of Chemical and Material Engineering, Jiangnan University, Wuxi 214122, China*
[3] *Research Center for Analysis and Measurement, Donghua University, Shanghai 201620, China*
[4] *Bristol Composites Institute (ACCIS), Department of Aerospace Engineering, Queen's Building, University of Bristol, University Walk, Bristol, BS8 1TR, UK*



**Received:** 17 August 2020 / **Revised:** 6 October 2020 / **Accepted:** 27 October 2020

## ABSTRACT

Despite the high theoretical specific capacity, the main challenges of rechargeable lithium-sulfur (Li-S) batteries, including the unceasing shuttle of soluble lithium polysulfides (LiPSs) and severe Li corrosion, seriously hinder their commercial and practical applications. Herein, a bifunctional polyvinyl alcohol/poly(lithium acrylate) (C-PVA/PAA-Li) composite nanofiber separator is developed to address the main challenges in Li-S batteries by simultaneously allowing rapid lithium ion transport and ionic shielding of polysulfides. The C-PVA/PAA-Li composite nanofiber membrane is prepared via the facile electrospinning strategy, followed by thermal crosslinking and *in-situ* lithiation processes. Differing from the conventional Celgard-based coating methods accompanied by impaired lithium ion transport efficiency, the C-PVA/PAA-Li composite nanofiber membrane possesses well-developed porous structures and high ionic conductivity, thus synergistically reducing the charge transfer resistance and inhibiting the growth of lithium dendrites. The resulting Li-S batteries exhibit an ultra-low fading rate of 0.08% per cycle after 400 cycles at 0.2 C, and a capacity of 633 mA·h·g$^{-1}$ at a high current density of 3 C. This study presents an inspiring and promising strategy to fabricate emerging dual-functional separators, which paves the pathway for the practical implementation of ultra-stable and reliable Li-S battery systems.

## KEYWORDS

nanofiber separator, electrospinning, ionic shielding, dendrite-free, lithium-sulfur battery

## 1 Introduction

The rapid development of portable electronics and emerging of electric vehicles give rise to an urgent demand for rechargeable batteries with high energy densities and long-term cycle life [1–4]. Compared to the traditional lithium-ion batteries, lithium-sulfur (Li-S) batteries are regarded as a promising candidate for next-generation energy storage devices due to their high theoretical specific capacity (1,675 mA·h·g$^{-1}$) and energy density (2,567 W·h·kg$^{-1}$) [5–7]. Li-S batteries have attracted considerable attention in recent decades owing to the additional merits of the higher safety than lithium-oxygen/air batteries, as well as abundance, low cost and environmentally-friendliness of sulfur as cathode [8–10].

However, the practical and commercial applications of Li-S batteries have been immensely hindered by the main challenges including the insulating nature of sulfur, large volumetric change of cathode, Li corrosion, and "shuttle effect" of Li polysulfides (LiPSs) [11–13]. Currently, on account of the low electronic or ionic conductivities of S ($\delta = 5 \times 10^{-30}$ S·cm$^{-1}$) and $Li_2S$ ($\delta = 10^{-13}$ S·cm$^{-1}$), conductive additives such as Super P, graphene, and carbon nanotubes are incorporated into cathode materials to enhance the electron transfer and guarantee sufficient electrochemical reactions while weakening the overall energy density [14]. Additionally, well-designed nanocomposite cathodes with these conductive additives are prone to collapse during the charge–discharge processes, resulting in the unsatisfactory advancement of S cathode design. Meanwhile, the corrosion of Li anode is attributed to side reactions with electrolyte and Li dendrites growth during Li plating/stripping processes, causing poor cycling performance and safety problems of these batteries [15]. Most importantly, LiPSs ($Li_2S_n$, $n \geq 4$) are inclined to dissolve during the discharge process. Subsequently, these polysulfides which migrate through the separator from cathode to anode, are directly reduced into insoluble $Li_2S_2$ and $Li_2S$ deposited on the anode surface. This occurrence is called the notorious "shuttle effect", leading to the loss of active materials and a serious reduction in the

Address correspondence to yuee_miao@dhu.edu.cn

Coulombic efficiency [16]. Therefore, the effective confinement of the intermediate LiPSs within the cathode side is critical to achieving efficient reversible electrochemical reactions and practical applications of Li-S batteries [17–19].

In the cell configuration, the sulfur cathode and Li metal anode are separated by an electrically insulating separator that plays a key role in preventing internal short circuits and maintaining lithium ion ($Li^+$) transport during the charge–discharge processes [20–22]. The essence of "shuttle effect" is the process that intermediate LiPSs continuously penetrate the separator during the charge–discharge processes, causing continuous loss of active substances and severe side reactions. Therefore, one of the most effective and fundamental ways to prevent the "shuttle effect" is to develop functional separators that can effectively confine soluble LiPSs in the sulfur cathode [23–25]. A variety of functionalized novel designs of polyethylene/polypropylene-based composite separators have been proposed to address the numerous challenges in Li-S batteries [26]. Among them, the carbon nanomaterials with a large specific surface area and an excellent electrical conductivity are widely used as the physical trap for LiPSs [27–32]. However, their intrinsic non-polarity determines their weak interactions with the polar LiPSs, thus greatly hindering the achievement of satisfactory capacity. Conversely, "adsorption coatings" with strong chemical affinities (e.g. metal oxides, metal sulfides, covalent organic frameworks, etc.) can provide strong chemical anchoring toward LiPSs [33–37]. Nonetheless, their poor conductivity will lead to inefficient electron transfer efficiency during charge–discharge processes. In addition, the coating strategy, either through physical confinement or chemical adsorption, will inevitably block the porous structure of the separators, resulting in a retarded $Li^+$ migration and a significant drop in the battery capacity [38–40]. Hence, it is very meaningful but challenging to simultaneously inhibit the LiPSs diffusion and maintain efficient transport pathways for $Li^+$.

Polyvinyl alcohol (PVA) is a water-soluble, biodegradable and nontoxic polymer which can be used in many industrial fields such as adhesives, textiles, fuel cells and lithium batteries [41, 42]. In recent years, PVA-based materials have also been reported as separator [43] or binder [44] for Li-S battery applications. In addition to its stability in the organic electrolyte, PVA possesses better thermal stability than those of the polyolefin-based separators. More importantly, PVA can be applied as the skeleton to graft functional groups and build three-dimensional network through the cross-linking esterification reactions between its hydroxyl groups and other groups (e.g., the carboxyl groups of polyacrylic acid) for Li-S battery separators [43]. As for poly(lithium acrylate) (PAA-Li), it has been generally considered as an attractive electrode binder due to its adhesion properties, stable physicochemical properties and intrinsic conductivity of ionic dissociation [45]. Interestingly, a flexible PAA-Li layer has been introduced by an *in-situ* reaction between Li metal and polyacrylic acid (PAA) to stabilize Li plating/stripping and restrain Li dendrite growth in lithium metal batteries [46]. Besides suppressing the dendrites formation, the electronegative $COO^-$ groups in PAA-Li could provide electrostatic repulsion to anionic LiPSs, which effectively prevented the active material loss caused by "shuttle effect".

Herein, a crosslinked polyvinyl alcohol/poly(lithium acrylate) (C-PVA/PAA-Li) composite nanofiber membrane is employed in this work to establish a dual-functional separator for simultaneous inhibition of Li dendrites and ionic shielding of polysulfides, which can not only efficiently immobilize the lithium polysulfides but also facilitate the uniform $Li^+$ flux. The thermally crosslinked polyvinyl alcohol/polyacrylic (C-PVA/PAA) composite nanofiber membrane with significantly improved mechanical strength and stability was obtained through the combination of electrospinning and heat treatment (Fig. 1). Subsequently, *in-situ* lithiation of the –COOH groups into –COOLi in PAA was carried out in a LiOH solution, thus achieving the bifunctional C-PVA/PAA-Li. Benefiting from the interpenetrating nanofibrous network structure and excellent ionic conductivity of PAA-Li, the $Li^+$ migration is greatly accelerated, and the uneven growth of Li dendrites is effectively suppressed. Furthermore, the negatively charged electrostatic barrier of C-PVA/PAA-Li composite can effectively inhibit the shuttling of LiPSs. Therefore, the battery assembled by C-PVA/PAA-Li separator displays high rate capacity of 633 $mA{\cdot}h{\cdot}g^{-1}$ at 3 C, and excellent cycle stability of only 0.08% decay per cycle after 400 cycles at 0.2 C, which further confirms the great potentials of the uniquely designed C-PVA/PAA-Li composite nanofiber separator in enhancing the battery performance and promoting large-scale applications of Li-S batteries in the future.

## 2 Experimental section

### 2.1 Materials

PVA ($M_W$ ≈ 89,000–98,000) and PAA ($M_W$ ≈ 450,000) were

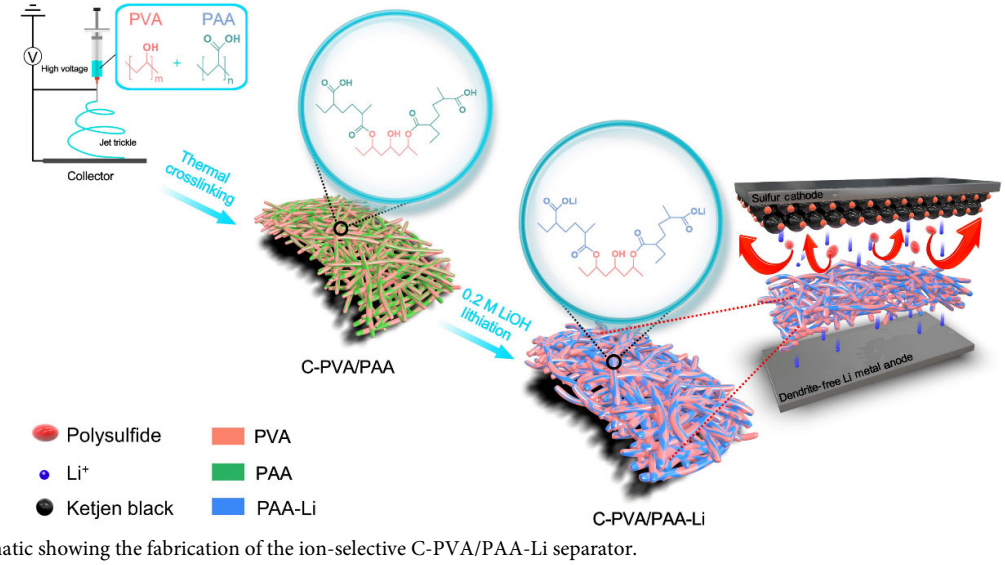


**Figure 1** Schematic showing the fabrication of the ion-selective C-PVA/PAA-Li separator.

purchased from Sigma-Aldrich Co., Ltd. Lithium hydroxide (anhydrous, 100G) was supplied by J&K Scientific Ltd. Ketchen black was provided by Suzhou Yi Longsheng Energy Technology Co., Ltd. All the chemicals were used without further purification.

### 2.2 Preparation of C-PVA/PAA composite nanofiber membrane

A transparent solution of 5 wt.% PVA was prepared by stirring PVA powder in ultra-pure water at 95 °C for 5 h and then cooling to room temperature. Subsequently, PAA was dissolved in the above PVA aqueous solution and stirred at room temperature for 24 h to obtain the electrospinning solution of PVA/PAA with a mass ratio of 5:7.5. The solution was then loaded into a 5 mL syringe and pumped to a needle tip at a flow rate of 0.08 mm·min$^{-1}$. The applied voltage was set at 18 kV and the distance between the needle tip and the collector was fixed at 15 cm. The electrospinning conditions were constantly monitored at an ambient temperature of 25 °C and the relative humidity of 35% ± 3%. Then, the as-prepared nanofiber membrane was placed in a high-temperature oven at 120 °C for 3 h for the crosslinking reactions between PVA and PAA. Finally, the crosslinked composite nanofiber membrane was dried at 60 °C for 24 h and named as C-PVA/PAA.

### 2.3 Preparation of C-PVA/PAA-Li and C-PVA/PAA-$H_2O$ separators

The C-PVA/PAA composite nanofiber membrane was lithiated with a LiOH solution. Typically, a C-PVA/PAA nanofiber membrane of approximately 4 cm × 4 cm was immersed in a 0.2 M LiOH solution for 10 min and then washed three times with ultra-pure water. Subsequently, the C-PVA/PAA-Li composite nanofiber separator was obtained by drying at 50 °C for 24 h. As a comparison, the same process was carried out using ultra-pure water instead of 0.2 M LiOH solution to obtain a C-PVA/PAA-$H_2O$ separator.

### 2.4 Preparation of the S/C cathode

A mixture of sulfur powder (60 wt.%), Ketchen Black (30 wt.%) and PVDF (10 wt.%) was well-stirred in *N*-methyl pyrrolidone solvent and then casted onto an aluminum foil. The resulting electrode was dried at 50 °C under vacuum for 12 h and cut into a circular shape with a diameter of 12 mm and a sulfur loading of 1.5–2.0 g·cm$^{-2}$.

### 2.5 Visual diffusion experiment of LiPSs

The visual diffusion test of LiPSs was conducted in a transparent H-type cell. The $Li_2S_6$ solution used in the penetration experiment was prepared by mixing sulfur powder and $Li_2S$ (5:1 by mole) in 1,3-dioxolane (DOL)/1,2-dimethoxyethane (DME) (v/v = 1:1) solution under vigorous stirring overnight. In the subsequent process, one chamber was filled with 0.1 M $Li_2S_6$ solution, while the other chamber was added with DOL/DME (v/v = 1:1). During the diffusion test, an H-type cell was separated by a C-PVA/PAA-Li separator to suppress the migration of LiPSs. As comparison, the H-type cell with a Celgard separator was synchronously tested.

### 2.6 Characterization

Optical microscopy images of the precursor solution for electrospinning were taken using an microscope (Olympus BX53M). Scanning electron microscopy (SEM) images were obtained on a scanning electron microscope (Hitachi S-4800), operated at 20 kV. The pore size distribution (PSD) of the separators was recorded on a PMI porometer (Porometer CFP 1300) at 0–300 psi. The tensile strength and tensile modulus were evaluated using a universal testing machine (AG-5000G, Shimadzu, Japan) at room temperature and a crosshead speed of 5 mm·min$^{-1}$. For all tensile tests, the sample strips were cut randomly from any direction from a complete nanofiber membrane or the commercial Celgard separator. The contact angle tester (Dataphysics OCA40 Micro) was applied to determine the surface wettability of the separators. Thermogravimetric analysis (TGA) was recorded with a thermal analyzer (Q5000IR) at a heating rate of 10 °C·min$^{-1}$ in air atmosphere. Fourier transform infrared (FTIR) spectra were acquired by an FTIR spectrometer (NicoletIn10MX/Nicolet6700) with an attenuated total reflectance (ATR) accessory.

The porosity of the separators was explored by the liquid absorption method and calculated according to the following equation

$$\text{Porosity} = \frac{W_w - W_0}{\rho_1 V} \quad (1)$$

The density of the separators was also obtained based on the following formula [47]

$$\text{Density}(\rho) = \frac{W_0}{V} \quad (2)$$

where $W_0$ represents the weight of the dry separator, $W_w$ is the weight of the separator immersed in 1,3-dioxolane (DOL) for 1 h, $\rho_1$ and $V$ represent the density of DOL and the volume of the separator, respectively.

The electrolyte uptake (EU) and retention (ER) of different separators were calculated according to the following equations

$$\text{Electrolyteuptake(EU)} = \frac{W_1 - W_0}{W_0} \times 100\% \quad (3)$$

$$\text{Electrolyteretention(ER)} = \frac{W_X - W_0}{W_1 - W_0} \times 100\% \quad (4)$$

where $W_0$ and $W_1$ represent the original weight and the weight of the separator immersed in electrolyte for 1 h, respectively. Then, the separator was placed in an oven at 50 °C to measure the equilibrium weight ($W_x$) in a series of times.

The ion exchange capacity (IEC, mmol·g$^{-1}$) was measured by a classical titration method. The separator was initially equilibrated in a 5 mol·L$^{-1}$ NaCl solution for 12 h to release protons in an exchange reaction with $Na^+$. Then, the amount of remaining $H^+$ in the above solution was titrated with 0.1 mol·L$^{-1}$ NaOH after the separator was removed, with a PHS-3E pH meter to determine the end of the neutralization reaction. The IEC values were calculated as follows [47]

$$\text{IEC} = (\Delta V_{\text{NaOH}} \times C_{\text{NaOH}}) \div W_0 \quad (5)$$

where $\Delta V_{\text{NaOH}}$ is the volume of the consumed NaOH solution, $C_{\text{NaOH}}$ is the concentration of NaOH solution (0.1 mol·L$^{-1}$), and $W_0$ corresponds to the weight of the dry separators.

### 2.7 Electrochemical tests

The standard CR2032 coin Li-S batteries equipped with various separators were fabricated in an argon-filled glove box using a sulfur cathode and a metal Li anode. In all experiments, 1 M bis-(trifluoromethane)sulfonamide lithium (LiTFSI) without $LiNO_3$ in a mixture of DME and DOL (v/v, 1:1) was used as the electrolyte with an electrolyte/sulfur ratio of 23 μL·mg$^{-1}$. For comparison, the Li-S battery was also assembled at a lower electrolyte/sulfur ratio of 13 μL·mg$^{-1}$. Galvanostatic charge–

discharge curves were collected on a NEWARE instrument between 1.7 and 2.8 V vs. $Li^+$/Li under various current densities. The electrochemical impedance spectroscopy (EIS) and cyclic voltammetry (CV) measurements were carried out on a CHI660E electrochemical workstation in the potential window of 1.7–2.8 V vs. $Li^+$/Li and frequency of 0.1–$10^5$ Hz, with a scan rate of 0.5 mV·$s^{-1}$. The ionic conductivity was tested by applying the electrolyte-saturated separator between two stainless steel electrodes in a coin-type battery and calculated according to the following equation

$$\sigma = \frac{L}{R \times A} \tag{6}$$

where $\sigma$ represents the ionic conductivity, $R$ is the bulk resistance, $L$ and $A$ represent the thickness and area of the separator, respectively [48]. The $Li^+$ migration number ($t_{Li^+}$) of the separator was measured by the chronoamperometry at a constant step potential of 10 mV in a Li|Li symmetric battery [49]. The specific values were calculated from the ratio between the steady-state current ($I_s$) and the initial-state current ($I_0$) according to the following equation

$$t_{Li^+} = I_s/I_0 \tag{7}$$

$Li^+$ diffusion coefficient ($D_{Li^+}$) was evaluated by a series of cyclic voltammetry tests from 0.05 to 0.5 mV·$s^{-1}$, with the peak current data analyzed by the Randles-Sevick equation

$$I_p = 2.69 \times 10^5 n^{1.5} A D_{Li^+}{}^{0.5} C_{Li} v^{0.5} \tag{8}$$

in which $I_p$ represents the different peak current (A), $n$ is the number of electrons involved in Li-S battery reaction ($n$ = 2), $A$ is the area of the electrode ($cm^2$), $C_{Li}$ refers to the $Li^+$ concentration (mol·$L^{-1}$) and $v$ stands for the scanning rate (V·$s^{-1}$). Besides, the $Li^+$ diffusion coefficient ($D_{Li^+}$) can be further explored based on the linear diffusion of the EIS results in the low-frequency region

$$D_{Li^+} = \frac{R^2T^2}{0.5A^2n^4F^4C_{Li^+}{}^2\sigma^2} \tag{9}$$

$$Z' = R_e + R_{ct} + \sigma\omega^{-0.5} \tag{10}$$

where $A$ is the surface area of the cathode, $R$ is the gas constant, $T$ is the absolute temperature, $F$ is the Faraday constant, and $\sigma$ represents the slope of an approximately linear distribution between $Z'$ and the square root of the frequency ($\omega^{-0.5}$) in the low-frequency region [49].

## 3 Results and discussion

With the hydrophilic PVA and PAA being uniformly co-dissolved in water (Fig. S1 in the Electronic Supplementary Material (ESM)), a simple and efficient electrospinning technique is adopted in combination with thermal crosslinking treatment to prepare the C-PVA/PAA composite nanofiber membrane. The morphology of the composite nanofibers is not affected during the thermal crosslinking process. Both of PVA/PAA and C-PVA/PAA composite nanofibers show smooth surface morphology with diameters ranging from 0.60 to 0.80 μm (Figs. S2(a) and S2(b) in the ESM). Compared to PVA/PAA, interfibrous bonding occurs in C-PVA/PAA derived from the crosslinking reaction, which results in a reduced porosity of 88.7% and a more concentrated pore size distribution around 1.60 μm (Figs. S3(a) and S3(b), and Table S1 in the ESM). After lithiation, the diameter of C-PVA/PAA-Li nanofibers increases to 0.67–0.85 μm (Fig. 2(a)), which is mainly attributed to the swelling of the composite nanofibers during the LiOH solution treatment. In addition, the C-PVA/PAA-Li composite nanofibers accumulate more tightly after soaking in LiOH aqueous solution, leading to largely reduced porosity (72.4%, Table S1 in the ESM) and pore size (1.30 μm, the inset of Fig. 2(a)). In order to exclude the effect of aqueous solvents on the pore structure of C-PVA/PAA nanofiber membrane, ultra-pure water was used instead of LiOH solution for post-treatment, thus resulting in the composite membrane of C-PVA/PAA-$H_2O$. As shown in Fig. S2(c) in the ESM, the C-PVA/PAA-$H_2O$ nanofibers become distorted and closely packed, indicating that the treatment of aqueous solvent will also lead to a decrease in the pore size (1.07 μm, Fig. S3(c) in the ESM) and porosity (71.2%, Table S1 in the ESM) of the C-PVA/PAA-$H_2O$ nanofiber

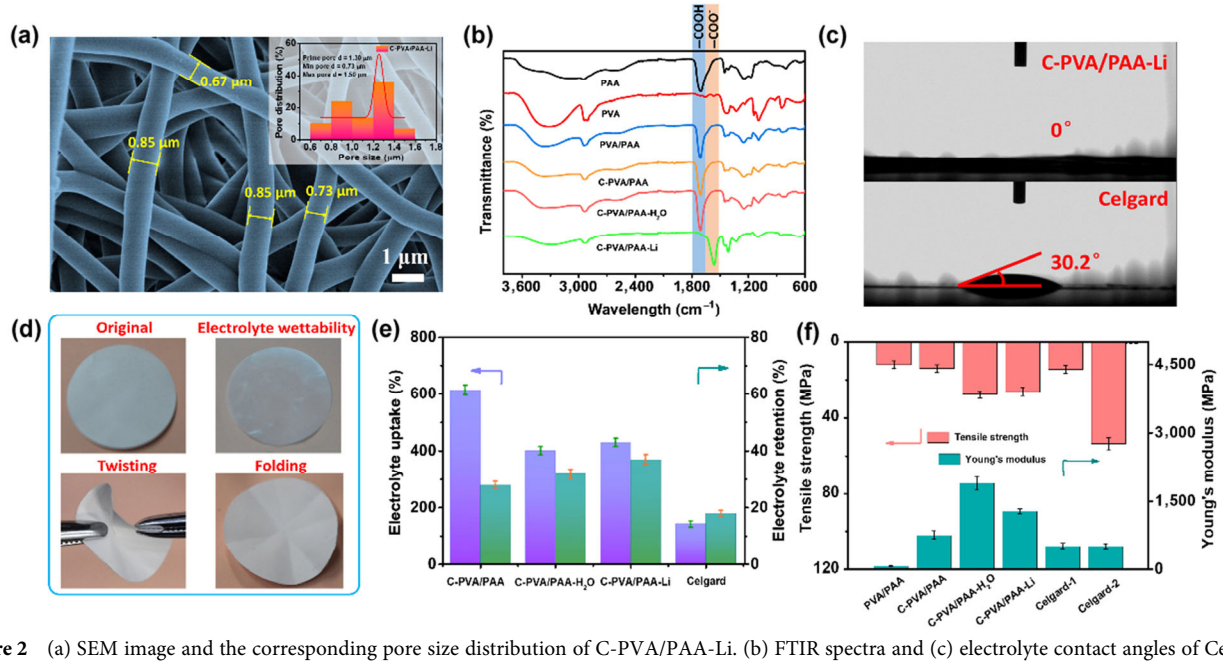


**Figure 2** (a) SEM image and the corresponding pore size distribution of C-PVA/PAA-Li. (b) FTIR spectra and (c) electrolyte contact angles of Celgard and C-PVA/PAA-Li. (d) Folding/twisting tests showing excellent flexibility and wettability of C/PVA/PAA-Li separator. (e) Electrolyte uptake and retention, and (f) mechanical properties of different samples.

membrane. However, the PVA/PAA nanofibers without crosslinking dissolve immediately after immersion in water (Fig. S4 in the ESM). To reveal the exact contents of –OH and –COOH groups on the nanofiber membranes, the ion exchange capacity (IEC) value is determined by acid-base titration method. The almost same IEC values for C-PVA/PAA (0.56 mmol·g$^{-1}$) and C-PVA/PAA-$H_2O$ (0.57 mmol·g$^{-1}$) separators indicate the stable content of –OH and –COOH groups during aqueous solvent treatment (Fig. S5 in the ESM). Then, FTIR spectroscopy is used to analyze the interactions between PVA and PAA, and confirm the lithiation efficiency of the C-PVA/PAA composite nanofiber membrane. As shown in Fig. 2(b), the vibrating bands of PVA are observed at 1,428, 2,918 and 2,935 cm$^{-1}$, attributed to the asymmetric stretching, symmetric stretching and bending vibrations of $-CH_3$, respectively. The most characteristic peak of PVA is located around 3,300 cm$^{-1}$, belonging to the strong stretching vibration of –OH groups. In addition, the characteristic vibration of carbonyl (–C=O) in PAA appears at about 1,704 cm$^{-1}$, with a broad band at 3,700–2,800 cm$^{-1}$ ascribed to the hydrogen bonding interactions between –COOH groups [21]. After the crosslinking between PAA and PVA, the stretching vibration of –C=O in PAA shifts to 1,714 cm$^{-1}$ while the relative absorption intensity of –OH group at 3,000–3,700 cm$^{-1}$ decreases, indicating the completion of the esterification reactions between the –OH of PVA and –COOH of PAA during thermal treatment [50]. After lithiation with a LiOH solution, the stretching vibration of –C=O in –COOH migrates to 1,564 cm$^{-1}$, revealing the formation of –COOLi in C-PVA/PAA-Li.

The C-PVA/PAA-Li composite nanofiber membrane not only has a much higher porosity than that of the commercial Celgard separator but also exhibits excellent electrolyte wettability with a contact angle of 0°, while the Celgard separator is difficult to be completely infiltrated by electrolytes (Fig. 2(c) and Fig. S6 in the ESM). As further indicated in Fig. 2(d), the immediate infiltration of liquid electrolyte dropping on C-PVA/PAA-Li membrane proves its relatively high hydrophilic surface toward liquid electrolyte into the internal nanofibrous network. In addition to the quite high porosity, the polar –OH and –COOLi groups of C-PVA/PAA-Li separator largely favor its compatibility with polar electrolyte. Thus, the electrolyte absorption (430%) and retention (37%) of the C-PVA/PAA-Li separator are obtained to be twice higher than those of the polyolefin-based Celgard separator which suffers from nonpolar nature and low surface energy (Fig. 2(e) and Fig. S7 in the ESM). Flexibility and mechanical strength are another two key features of separators, which can prevent the internal short circuits caused by dendrite growth and play important roles in battery safeties. Significantly, the crosslinking reaction between PVA and PAA can notably improve the mechanical strength and stability of the C-PVA/PAA composite nanofiber membrane. As shown in Fig. 2(d), the C-PVA/PAA-Li nanofiber separator infiltrated with electrolyte shows no obvious damage when it is subjected to different bending conditions of random folding or twisting. To more accurately demonstrate the mechanical properties, tensile tests are performed on different separators (Fig. 2(f) and Fig. S8(a) in the ESM). Unfortunately, the commercial Celgard exhibits significant anisotropy with the tensile strength of only 14.6 MPa and Young's modulus of 511.1 MPa in the weak direction (Table S2 in the ESM), which may be unsuitable for random stress conditions within the batteries. In contrast, both of the C-PVA/PAA-Li and C-PVA/PAA-$H_2O$ separators exhibit excellent isotropic tensile strength of 26.5 MPa, 27.9 MPa and Young's modulus of 1,274.9 MPa, 1,891.9 MPa, respectively, which are much higher than those of Celgard. The slightly inferior properties of C-PVA/PAA-Li compared to C-PVA/PAA-$H_2O$ can be attributed to the weakened hydrogen bonding interactions after the transition of PAA to PAA-Li. Therefore, the C-PVA/PAA-Li separator with excellent isotropic mechanical properties shows great potentials in dealing with the complex environment inside the batteries. The thermal stability of the nanofiber separators in the air is shown in Fig. S8(b) in the ESM, which indicates that alkali metal polyacrylate is stable in normal electrode drying and working environments.

The $Li^+$ conductivity is a major parameter for separators, playing a key role in determining the electrochemical performances of Li-S batteries. Hence, the bulk resistance ($R_b$) of the separator is explored from the real part ($Z'$) of the complex impedance when the imaginary part ($Z''$) disappears (Fig. S9 and Table S3 in the ESM). Furthermore, the $Li^+$ transfer number and ionic conductivity of various separators are shown in Fig. 3(a) and Fig. S10 in the ESM. Limited by the low porosity (40.1%) and $Li^+$ insulation property, the Celgard separator displays very low ionic conductivity (0.012 mS·cm$^{-1}$) and $Li^+$ transfer number (0.44). In contrast, ascribed to the highly porous interpenetrating network structure, high ionic conductivities of 0.023, 0.014, 0.054 mS·cm$^{-1}$ and large $Li^+$ transfer numbers of 0.60, 0.57 and 0.70 are achieved for C-PVA/PAA, C-PVA/PAA-$H_2O$, and C-PVA/PAA-Li, respectively. As the treatment of aqueous solvent results in a decreased porosity, $Li^+$ migration in C-PVA/PAA-$H_2O$ is hindered compared with C-PVA/PAA. Nevertheless, C-PVA/PAA-Li still maintains a significantly enhanced ionic conductivity because the fast $Li^+$ exchange channels constructed by the introduction of –COOLi will efficiently reduce the migration barrier and accelerate $Li^+$ transfer within the separator network (Fig. 3(b)).

Subsequently, the electrochemical kinetics of the coin-type Li-S battery was investigated by electrochemical impedance spectroscopy (EIS). As displayed in Fig. 3(c) and Table S4 in the ESM, the charge transfer resistance ($R_{ct}$) of batteries assembled

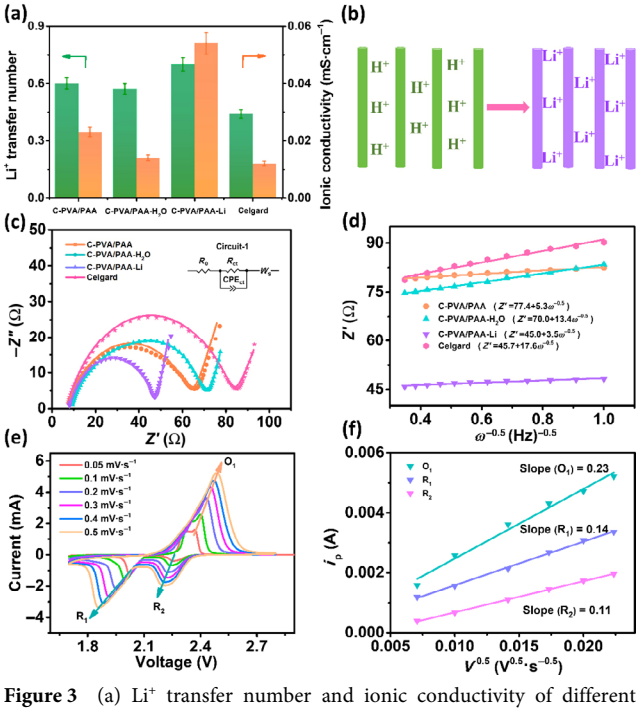


**Figure 3** (a) $Li^+$ transfer number and ionic conductivity of different separators. (b) Schematic illustration of C-PVA/PAA-Li separator promoting $Li^+$ transport. (c) EIS of Li-S batteries with various separators and (d) the relationship between $Z'$ and $\omega^{-0.5}$ at the low-frequency region. (e) CV curves under different scanning rates and (f) the corresponding linear fits of the peak currents for Li-S batteries with C-PVA/PAA-Li.

with C-PVA/PAA, C-PVA/PAA-$H_2O$, C-PVA/PAA-Li, and Celgard separators are 58.0, 65.2, 40.1, and 76.8 Ω, respectively. This indicates that the C-PVA/PAA-Li separator can effectively reduce the resistance during $Li^+$ migration and achieve rapid electrochemical reaction kinetics. According to Eqs. (9) and (10), there is a linear relationship between $Z'$ and the square root of the frequency ($\omega^{0.5}$) in the low-frequency region, where the square of the slope is inversely proportional to the $Li^+$ diffusion coefficient ( $D_{Li^+}$ ). As shown in Fig. 3(d), all of the slopes for C-PVA/PAA (5.3), C-PVA/PAA-$H_2O$ (13.4), and C-PVA/PAA-Li (3.5) are lower than that (17.6) of Celgard, which are in good accordance with the corresponding results of $Li^+$ transfer number. Furthermore, in order to obtain $D_{Li^+}$ at different redox stages of Li-S batteries assembled with C-PVA/PAA, C-PVA/PAA-$H_2O$, C-PVA/PAA-Li and Celgard separators, a series of cyclic voltammetry (CV) tests under different scan rates are performed in Fig. 3(e) and Figs. S11(a)–S11(c) in the ESM. With a linear relationship between the peak current ($I_p$) and the square root of the scan rate ($V^{0.5}$) (Fig. 3(f) and Figs. S11(d)–S11(f) in the ESM), the specific $D_{Li^+}$ values are obtained according to the Randles-Sevick equation [51]. As listed in Table S5 in the ESM, the diffusion coefficients of C-PVA/PAA-Li separators are determined as ($R_1$) = 7.15 × $10^{-14}$ $cm^2 \cdot s^{-1}$, ($R_2$) = 2.65 × $10^{-14}$ $cm^2 \cdot s^{-1}$, and ($O_1$) = 1.64 × $10^{-14}$ $cm^2 \cdot s^{-1}$, which are much higher than those of the Celgard separator. The above results prove that the well-developed interpenetrating porous structure and high ionic conductivity of C-PVA/PAA-Li separator can significantly enhance the electrochemical reaction kinetics of Li-S batteries.

In order to verify the potential application of C-PVA/PAA-Li separator as an electrostatic repulsion barrier for LiPSs, visual diffusion experiments are performed to clearly demonstrate the migration process of LiPSs. An H-type glass cell is employed to hold 0.05 M $Li_2S_6$ solution in the left chamber and DOL/DME solvent without $Li_2S_6$ in the right side, while the two chambers are separated by a Celgard or C-PVA/PAA-Li separator, respectively. The right chamber of the cell with Celgard separator shows a significant color change after 2 h and finally turns brown after 48 h, indicating that LiPSs can easily diffuse through the Celgard separator (Fig. 4). In sharp contrast, the migration of LiPSs can be effectively suppressed with C-PVA/PAA-Li separator, with the right chamber showing no obvious color change during 24 h. Then, the detailed electrochemical behaviors of Li-S batteries are further investigated by CV at 0.1 $mV \cdot s^{-1}$ (Fig. 5(a)). Two cathodic peaks are determined

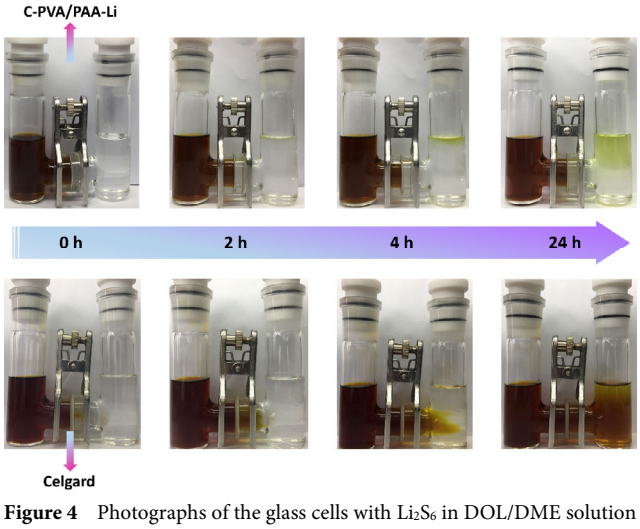


**Figure 4** Photographs of the glass cells with $Li_2S_6$ in DOL/DME solution and pure DOL/DME solvent in the left and right chambers, respectively, separated by a Celgard or C-PVA/PAA-Li separator.

around 2.24 and 2.0 V, corresponding to the reduction from cyclic-$S_8$ to long-chain LiPSs and further conversion to $Li_2S_2$/$Li_2S$, respectively. In the subsequent anodic scan process, the two overlapped peaks appearing at 2.35 and 2.40 V are attributed to the re-formation of $Li_2S_n$ ($n > 2$) and cyclo-$S_8$, respectively. The nearly overlapping CV curves after different cycles indicate the highly reversible redox conversion and excellent stability contributed by the C-PVA/PAA-Li separator.

In order to investigate the specific capacities of the batteries employing different separators, the rate performance is tested under current densities of 0.1–3 C (Fig. 5(b)). When the traditional Celgard is applied, an initial discharge capacity of 1,004 $mA \cdot h \cdot g^{-1}$ is achieved at 0.1 C, and then rapidly decays to 191 $mA \cdot h \cdot g^{-1}$ at 3 C, which is ascribed to the severe shuttling of LiPSs. On the contrary, benefitting from the three-dimensional network structure of nanofiber membranes and the electrostatic repulsion toward LiPSs, the rate performance of Li-S batteries assembled with nanofiber separators has a significant increase. For C-PVA/PAA and C-PVA/PAA-$H_2O$, the capacities under a high current density of 3 C are 434 and 498 $mA \cdot h \cdot g^{-1}$, respectively. However, as the excessively high porosity (88.7%) of the C-PVA/PAA separator may also accelerate the shuttling of LiPSs, the C-PVA/PAA-$H_2O$ separator with a reduced porous structure demonstrates stronger electrostatic repulsion and higher rate capacity. Significantly, by introducing the ion-selective C-PVA/PAA-Li separator, the electrochemical performance has been greatly improved with an excellent initial capacity of about 1,482 $mA \cdot h \cdot g^{-1}$ at 0.1 C and an ultra-high rate capacity of 633 $mA \cdot h \cdot g^{-1}$ at 3 C, respectively. When the current density turns back to 1 C, the battery using C-PVA/PAA-Li separator remains a good reversible capacity of 729 $mA \cdot h \cdot g^{-1}$, indicating the robust reversibility and excellent rate performance. In addition, the rate performance of the Li-S battery assembled by C-PVA/PAA-Li was also evaluated at a lower electrolyte loading with the electrolyte/sulfur ratio of 13 $\mu L \cdot mg^{-1}$. As shown in Fig. S12 in the ESM, the initial capacity is up to 1,221 $mA \cdot h \cdot g^{-1}$ at 0.1 C. Furthermore, the capacity remains at 770, 596, 487, 369, and 254 $mA \cdot h \cdot g^{-1}$ when cycling at 0.2, 0.5, 1, 2 and 3 C, respectively. Compared with the battery assembled by C-PVA/PAA-Li separator at a high electrolyte/sulfur loading amount of 23 $\mu L \cdot mg^{-1}$ (Fig. 5(b)), it can be observed that the capacity retention is slightly decreased as the electrolyte loading decreases. Subsequently, the galvanostatic charge–discharge curves of batteries assembled with different separators are shown in Fig. 5(c) and Figs. S13(a)–S13(c) in the ESM, respectively. In accordance with the CV curves, two apparent discharge plateaus can be clearly observed under low current rates, indicating the particular multi-stage reduction processes of the sulfur cathode. For Celgard, C-PVA/PAA and C-PVA/PAA-$H_2O$, the voltages of the discharge plateaus drop significantly at 1–3 C (Figs. S13(a)–S13(c) in the ESM), which can be attributed to the severe polarization at high current densities. In contrast, the battery equipped with C-PVA/PAA-Li separator consistently keeps a small polarization voltage due to high ionic conductivity and $Li^+$ migration efficiency (Fig. 5(c)), which indicates the efficient maintenance of fast $Li^+$ exchange at high current densities. The above results evidently attribute to the fact that C-PVA/PAA-Li separator can not only effectively inhibit the shuttling of LiPSs by electrostatic repulsion, but also accelerate $Li^+$ migration to enhance the electrochemical reaction kinetics.

As shown in Figs. 5(d) and 5(e), the cyclability of batteries is further examined at different charge–discharge current densities of 0.2 and 1 C, after the activation at a low current rate of 0.05 C. Notably, the battery incorporating the C-PVA/

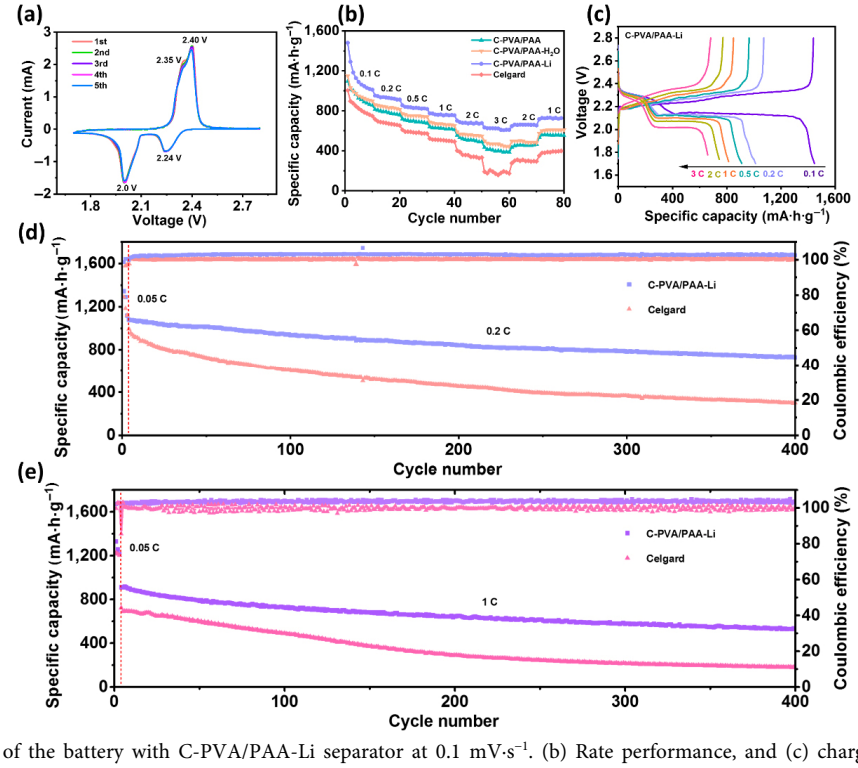


**Figure 5** (a) CV curves of the battery with C-PVA/PAA-Li separator at 0.1 mV·s$^{-1}$. (b) Rate performance, and (c) charge–discharge curves of the batteries with different separators at various current densities of 0.1–3 C. The long-term cycling performance of the batteries with C-PVA/PAA-Li and Celgard separators at (d) 0.2 C and (e) 1 C.

PAA-Li separator exhibits an ultra-low capacity fading of only 0.08% per cycle at a current density of 0.2 C, and remains 736 mA·h·g$^{-1}$ after 400 charge–discharge cycles, which are rather superior over lots of previous reports (Table S6 in the ESM). However, due to the continuous shuttling of LiPSs, the battery assembled by Celgard separator has a capacity of only 299 mA·h·g$^{-1}$ after circulating at 0.2 C, with the decay rate per cycle as high as 0.17%. Besides, the reversible capacity of the battery with C-PVA/PAA-Li at a high current density of 1 C also exhibits superior stability over Celgard, with 536 mA·h·g$^{-1}$ after 400 cycles at a fading rate of only 0.13% per cycle. The battery with C-PVA/PAA-Li separator also displays extremely high Coulombic efficiencies (> 99.5%) throughout the 400 cycles, indicating an effective blocking of soluble LiPSs.

It is well known that suppressing Li dendrites and ensuring long-term cycling performance of lithium metal anodes are the major challenges of Li-S batteries. Therefore, the morphology of lithium metal anodes of the Li-S batteries assembled with different separators is further investigated after 400 cycles at 0.2 C. For the battery assembled with Celgard, the Li anode shows a rough surface covered by sharp Li dendrites. Many large aggregates of dead Li species are also observed due to the corrosion of Li anode by LiPSs (Fig. 6(a)). However, the growth of Li dendrites is efficiently alleviated for the C-PVA/PAA and C-PVA/PAA-$H_2O$ cases (Figs. S14(a) and S14(b) in the ESM). Benefiting from the free migration of $Li^+$ in the high-porosity nanofiber membranes, the growth of lithium dendrites and corrosion of lithium metal anodes are suppressed. Significantly, when a C-PVA/PAA-Li separator is introduced, the lithium metal anode surface becomes very smooth without obvious corrosion due to its high ionic conductivity and good compatibility with lithium metal anode (Fig. 6(b)). Figure 6(c) illustrates the possible mechanism for the destruction of Li metal anode during the conventional Celgard operation. The easily diffused LiPSs will inevitably corrode the Li anode, thus resulting in the non-uniform $Li^+$ flux which forms

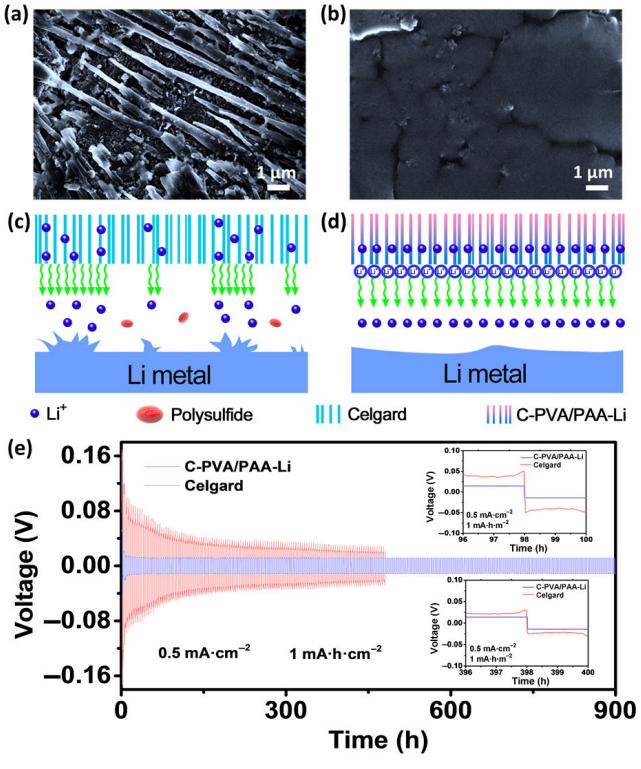


**Figure 6** SEM images of Li metal anodes with (a) Celgard and (b) C-PVA/PAA-Li separators after 500 cycles at 0.2 C. (c) Schematic showing the formation of lithium dendrites due to slow and uneven $Li^+$ deposition using Celgard separator. (d) C-PVA/PAA-Li separator guides the rapid and uniform deposition of $Li^+$ to avoid the formation of lithium dendrites. (e) Voltage–time profiles of Li|Li symmetric cells for C-PVA/PAA-Li and Celgard separators at 0.5 mA·cm$^{-2}$ with a capacity of 1 mA·h·cm$^{-2}$.

inhomogeneous Li deposition and ultimately leads to unstable cycle efficiency and poor service life of the Li metal anode. In

contrast, the strong electrostatic barrier of C-PVA/PAA-Li is effective in blocking LiPSs, which can efficiently prohibit the corrosion of Li metal and unusable dead Li species. In addition, the original non-uniform $Li^+$ flux can be redistributed through the ion-conducting composite nanofiber membrane to evenly deposit on the Li anode (Fig. 6(d)), thus providing an ideal strategy to simultaneously promote Li transfer and stabilize Li anode.

To gain insight into the effects of the separators on Li deposition, galvanostatic Li plating/stripping cycling test is carried out in Li|Li symmetric batteries. The battery with C-PVA/PAA-Li separator cycling at 1 $mA·cm^{-2}$ with a capacity of 1 $mAh·cm^{-2}$ produces a relatively high overpotential in the first few cycles due to the SEI formation and electrode activation (Fig. 6(e)). Subsequently, a low and stable overpotential of less than 25 mV is maintained within 900 h, indicating the formation of a stable SEI layer and uniform Li plating/stripping. In contrast, the overpotential of the Celgard-based battery gradually decreases from the initial 168 to 27 mV during the 480 h test, and finally goes short-circuit. This can be attributed to the continuous destruction and reformation of the SEI layer, and ultimately resulted in uncontrollable Li dendrite growth, which pierces the Celgard separator and causes the disruption to the batteries. At a higher current density of 1 $mA·cm^{-2}$ with a capacity of 2 $mA·h·cm^{-2}$, the differences in overpotential and long-term cycling stability become more obvious (Fig. S15 in the ESM). The Li|Li symmetrical battery assembled with Celgard exhibits a much higher voltage hysteresis (~ 315 mV) at the beginning of Li plating/peeling, followed by a distinct necking behavior. Obviously, the C-PVA/PAA-Li based battery maintains a stable overpotential of approximately 35 mV over 900 h without any voltage fluctuations, further proving that the C-PVA/PAA-Li composite nanofiber separator with high ionic conductivity can guide the uniform deposition of $Li^+$ for the achievement of lithium metal batteries with long cycle life and high safety.

The morphology and structural stability of C-PVA/PAA-Li composite nanofiber separator during the charge–discharge cycle of Li-S batteries are also tested. The smooth nanofiber morphology demonstrates the excellent stability of the C-PVA/PAA-Li membrane, ensuring adequate battery safety over long periods of electrochemical reactions (Fig. S16(a) in the ESM). Then, the FTIR spectra of C-PVA/PAA-Li separator under different electrochemical states are collected to explore their working mechanism in the charge–discharge reaction processes. Regardless of the discharging to 1.7 V or charging to 2.8 V, there is no change in the stretching vibration of –C=O in lithium carboxylate (–COOLi) at 1,564 $cm^{-1}$ (Fig. S16(b) in the ESM), indicating a stable dynamic equilibrium state between the –COOLi in C-PVAPAA-Li and free $Li^+$ contained inside the battery to guarantee the rapid $Li^+$ transport for achieving high power density Li-S batteries.

## 4 Conclusion

In this study, we have demonstrated a novel C-PVA/PAA-Li nanofiber separator for advanced Li-S batteries, which emphasizes the dual functions of an electrostatic repulsion barrier for LiPSs and the accelerated $Li^+$ migration feature. The C-PVA/PAA-Li composite nanofiber membrane exhibits a higher porosity, better electrolyte wettability and superior isotropic mechanical properties compared to commercial Celgard. Furthermore, C-PVA/PAA-Li possesses a high ionic conductivity (0.054 $mS·cm^{-1}$), $Li^+$ transfer number (0.7) and $Li^+$ diffusion coefficient ($1.35 \times 10^{-14}$ $cm^2·s^{-1}$ at oxidation peak), which contribute to the rapid electrochemical kinetics and low charge transfer resistance of Li-S batteries. As a result, the Li-S battery with C-PVA/PAA-Li separator demonstrates excellent cycling performance with an ultra-low capacity decay rate of 0.08% per cycle, and an outstanding rate performance of 633 $mAh·g^{-1}$ at 3 C. In addition, Li dendrite growth has been effectively inhibited during long-term stripping/plating cycling. This study demonstrates a prospective strategy to inhibit "shuttle effect" of LiPSs and Li dendrite growth via this bifunctional C-PVA/PAA-Li separator, which opens avenue towards the development of ultra-stable and high-performance Li-S batteries.

## Acknowledgements

The authors are grateful for the financial support from the National Natural Science Foundation of China (No. 21604010), the Natural Science Foundation of Shanghai (No. 18ZR1401600), "Chenguang Program" supported by Shanghai Education Development Foundation and Shanghai Municipal Education Commission (No. 16CG39), and Shanghai Scientific and Technological Innovation Project (No. 18JC1410600).

**Electronic Supplementary Material:** Supplementary material (optical microscopy and SEM images, pore size distributions, IEC values, electrolyte wettability, mechanical properties, and electrochemical performances of different separators) is available in the online version of this article at https://doi.org/10.1007/s12274-020-3213-y.

## References

[1] Liang, X.; Hart, C.; Pang, Q.; Garsuch, A.; Weiss, T.; Nazar, L. F. A highly efficient polysulfide mediator for lithium-sulfur batteries. *Nat. Commun.* **2015**, *6*, 5682.

[2] Ye, Y. F.; Song, M. K.; Xu, Y.; Nie, K. Q.; Liu, Y. S.; Feng, J.; Sun, X. H.; Cairns, E. J.; Zhang, Y. G.; Guo, J. H. Lithium nitrate: A double-edged sword in the rechargeable lithium-sulfur cell. *Energy Storage Mater.* **2019**, *16*, 498–504.

[3] Pei, F.; Lin, L. L.; Fu, A.; Mo, S. G.; Ou, D. H.; Fang, X. L.; Zheng, N. F. A two-dimensional porous carbon-modified separator for high-energy-density Li-S batteries. *Joule* **2018**, *2*, 323–336.

[4] Yan, C. Y.; Zhu, P.; Jia, H.; Zhu, J. D.; Selvan, R. K.; Li, Y.; Dong, X.; Du, Z.; Angunawela, I.; Wu, N. Q. et al. High-performance 3-D fiber network composite electrolyte enabled with Li-ion conducting nanofibers and amorphous PEO-based cross-linked polymer for ambient all-solid-state lithium-metal batteries. *Adv. Fiber Mater.* **2019**, *1*, 46–60.

[5] Zhu, J. D.; Zhu, P.; Yan, C. Y.; Dong, X.; Zhang, X. W. Recent progress in polymer materials for advanced lithium-sulfur batteries. *Prog. Polym. Sci.* **2019**, *90*, 118–163.

[6] Su, D. W.; Zhou, D.; Wang, C. Y.; Wang, G. X. Toward high performance lithium-sulfur batteries based on $Li_2S$ cathodes and beyond: Status, challenges, and perspectives. *Adv. Funct. Mater.* **2018**, *28*, 1800154.

[7] Peng, H. J.; Huang, J. Q.; Cheng, X. B.; Zhang, Q. Review on high-loading and high-energy lithium-sulfur batteries. *Adv. Energy Mater.* **2017**, *7*, 1700260.

[8] Hou, T. Z.; Xu, W. T.; Chen, X.; Peng, H. J.; Huang, J. Q.; Zhang, Q. Lithium bond chemistry in lithium–sulfur batteries. *Angew. Chem., Int. Ed.* **2017**, *56*, 8178–8182.

[9] Li, Z.; Han, Y.; Wei, J. H.; Wang, W. Q.; Cao, T. T.; Xu, S. M.; Xu, Z. H. Suppressing shuttle effect using Janus cation exchange membrane for high-performance lithium-sulfur battery separator. *ACS Appl. Mater. Interfaces* **2017**, *9*, 44776–44781.

[10] Su, C. C.; He, M. N.; Amine, R.; Chen, Z. H.; Amine, K. The relationship between the relative solvating power of electrolytes and shuttling effect of lithium polysulfides in lithium-sulfur batteries. *Angew. Chem., Int. Ed.* **2018**, *57*, 12033–12036.

[11] Song, Y. Z.; Cai, W. L.; Kong, L.; Cai, J. S.; Zhang, Q.; Sun, J. Y. Rationalizing electrocatalysis of Li-S chemistry by mediator design: Progress and prospects. *Adv. Energy Mater.* **2020**, *10*, 1901075.

[12] Shi, N. X.; Xi, B. J.; Feng, Z. Y.; Wu, F. F.; Wei, D. H.; Liu, J.; Xiong, S. L. Insight into different-microstructured ZnO/graphene-functionalized separators affecting the performance of lithium-sulfur batteries. *J. Mater. Chem. A* **2019**, *7*, 4009–4018.

[13] Cui, J. Y.; Li, Z. H.; Li, J. B.; Li, S.; Liu, J.; Shao, M. F.; Wei, M. An atomic-confined-space separator for high performance lithium-sulfur batteries. *J. Mater. Chem. A* **2020**, *8*, 1896–1903.

[14] Lei, T. Y.; Chen, W.; Lv, W. Q.; Huang, J. W.; Zhu, J.; Chu, J. W.; Yan, C. Y.; Wu, C. Y.; Yan, Y. C.; He, W. D. et al. Inhibiting polysulfide shuttling with a graphene composite separator for highly robust lithium-sulfur batteries. *Joule* **2018**, *2*, 2091–2104.

[15] Jin, C. B.; Zhang, W. K.; Zhuang, Z. Z.; Wang, J. G.; Huang, H.; Gan, Y. P.; Xia, Y.; Liang, C.; Zhang, J.; Tao, X. Y. Enhanced sulfide chemisorption using boron and oxygen dually doped multi-walled carbon nanotubes for advanced lithium–sulfur batteries. *J. Mater. Chem. A* **2017**, *5*, 632–640.

[16] Li, G. R.; Wang, S.; Zhang, Y. N.; Li, M.; Chen, Z. W.; Lu, J. Revisiting the role of polysulfides in lithium-sulfur batteries. *Adv. Mater.* **2018**, *30*, 1705590.

[17] Zhou, T. H.; Lv, W.; Li, J.; Zhou, G. M.; Zhao, Y.; Fan, S. X.; Liu, B. L.; Li, B. H.; Kang, F. Y.; Yang, Q. H. Twinborn $TiO_2$-TiN heterostructures enabling smooth trapping-diffusion-conversion of polysulfides towards ultralong life lithium-sulfur batteries. *Energy Environ. Sci.* **2017**, *10*, 1694–1703.

[18] Yu, J. J.; Liu, S. W.; Duan, G. G.; Fang, H.; Hou, H. Q. Dense and thin coating of gel polymer electrolyte on sulfur cathode toward high performance Li-sulfur battery. *Compos. Commun.* **2020**, *19*, 239–245.

[19] Chen, W.; Lei, T. Y.; Lv, W. Q.; Hu, Y.; Yan, Y. C.; Jiao, Y.; He, W. D.; Li, Z. H.; Yan, C. L.; Xiong, J. Atomic interlamellar ion path in high sulfur content lithium-montmorillonite host enables high-rate and stable lithium-sulfur battery. *Adv. Mater.* **2018**, *30*, 1804084.

[20] Rana, M.; Li, M.; Huang, X.; Luo, B.; Gentle, I.; Knibbe, R. Recent advances in separators to mitigate technical challenges associated with re-chargeable lithium sulfur batteries. *J. Mater. Chem. A* **2019**, *7*, 6596–6615.

[21] Zhu, X. B.; Ouyang, Y.; Chen, J. W.; Zhu, X. G.; Luo, X.; Lai, F. L.; Zhang, H.; Miao, Y. E.; Liu, T. X. *In situ* extracted poly(acrylic acid) contributing to electrospun nanofiber separators with precisely tuned pore structures for ultra-stable lithium-sulfur batteries. *J. Mater. Chem. A* **2019**, *7*, 3253–3263.

[22] Fang, R. P.; Zhao, S. Y.; Sun, Z. H.; Wang, D. W.; Cheng, H. M.; Li, F. More reliable lithium-sulfur batteries: Status, solutions and prospects. *Adv. Mater.* **2017**, *29*, 1606823.

[23] Fu, X. W.; Wang, Y.; Scudiero, L.; Zhong, W. H. A polymeric nanocomposite interlayer as ion-transport-regulator for trapping polysulfides and stabilizing lithium metal. *Energy Storage Mater.* **2018**, *15*, 447–457.

[24] Wu, F.; Zhao, S. Y.; Chen, L.; Lu, Y.; Su, Y. F.; Jia, Y. N.; Bao, L. Y.; Wang, J.; Chen, S.; Chen, R. J. Metal-organic frameworks composites threaded on the CNT knitted separator for suppressing the shuttle effect of lithium sulfur batteries. *Energy Storage Mater.* **2018**, *14*, 383–391.

[25] Wang, W.; Liao, C.; Liew, K. M.; Chen, Z. H.; Song, L.; Kan, Y. C.; Hu, Y. A 3D flexible and robust HAPs/PVA separator prepared by a freezing-drying method for safe lithium metal batteries. *J. Mater. Chem. A* **2019**, *7*, 6859–6868.

[26] Cheng, X. B.; Peng, H. J.; Huang, J. Q.; Wei, F.; Zhang, Q. Dendrite-free nanostructured anode: Entrapment of lithium in a 3D fibrous matrix for ultra-stable lithium–sulfur batteries. *Small* **2014**, *10*, 4257–4263.

[27] Song, J. J.; Zhang, C. Y.; Guo, X.; Zhang, J. Q.; Luo, L. Q.; Liu, H.; Wang, F. Y.; Wang, G. X. Entrapping polysulfides by using ultrathin hollow carbon sphere-functionalized separators in high-rate lithium-sulfur batteries. *J. Mater. Chem. A* **2018**, *6*, 16610–16616.

[28] Zhang, L. L.; Chen, X.; Wan, F.; Niu, Z. Q.; Wang, Y. J.; Zhang, Q.; Chen, J. Enhanced electrochemical kinetics and polysulfide traps of indium nitride for highly stable lithium-sulfur batteries. *ACS Nano* **2018**, *12*, 9578–9586.

[29] Li, J. H.; Wei, W.; Meng, L. J. Liquid-phase exfoliated-graphene-supporting nanostructural sulfur as high-performance lithium-sulfur batteries cathode. *Compos. Commun.* **2019**, *15*, 149–154.

[30] Shi, H. F.; Lv, W.; Zhang, C.; Wang, D. W.; Ling, G. W.; He, Y. B.; Kang, F. Y.; Yang, Q. H. Functional carbons remedy the shuttling of polysulfides in lithium-sulfur batteries: Confining, trapping, blocking, and breaking up. *Adv. Funct. Mater.* **2018**, *28*, 1800508.

[31] Tian, W. Z.; Xi, B. J.; Gu, Y.; Fu, Q.; Feng, Z. Y.; Feng, J. K.; Xiong, S. L. Bonding $VSe_2$ ultrafine nanocrystals on graphene toward advanced lithium-sulfur batteries. *Nano Res.* **2020**, *13*, 2673–2682.

[32] Zuo, X. T.; Zhen, M. M.; Wang, C. Ni@N-doped graphene nanosheets and CNTs hybrids modified separator as efficient polysulfide barrier for high-performance lithium sulfur batteries. *Nano Res.* **2019**, *12*, 829–836.

[33] Ghazi, Z. A.; Zhu, L. Y.; Wang, H.; Naeem, A.; Khattak, A. M.; Liang, B.; Khan, N. A.; Wei, Z. X.; Li, L. S.; Tang, Z. Y. Efficient polysulfide chemisorption in covalent organic frameworks for high-performance lithium-sulfur batteries. *Adv. Energy Mater.* **2016**, *6*, 1601250.

[34] Liu, B.; Huang, S. Z.; Kong, D. Z.; Hu, J. P.; Yang, H. Y. Bifunctional $NiCo_2S_4$ catalysts supported on a carbon textile interlayer for ultra-stable Li-S battery. *J. Mater. Chem. A* **2019**, *7*, 7604–7613.

[35] Luo, X.; Lu, X. B.; Zhou, G. Y.; Zhao, X. Y.; Ouyang, Y.; Zhu, X. B.; Miao, Y. E.; Liu, T. X. Ion-selective polyamide acid nanofiber separators for high-rate and stable lithium-sulfur batteries. *ACS Appl. Mater. Interfaces* **2018**, *10*, 42198–42206.

[36] Zhou, J.; Wang, Y. F.; Zhang, C. Synthesis and electrochemical performance of core-shell $NiCo_2S_4$@nitrogen, sulfur dual-doped carbon composites via confined sulfidation strategy in a polydopamine nanoreactor. *Compos. Commun.* **2019**, *12*, 74–79.

[37] Fan, Y.; Yang, Z.; Hua, W. X.; Liu, D.; Tao, T.; Rahman, M.; Lei, W. W.; Huang, S. M.; Chen, Y. Functionalized boron nitride nanosheets/graphene interlayer for fast and long-life lithium-sulfur batteries. *Adv. Energy Mater.* **2017**, *7*, 1602380.

[38] Wang, Z.; Feng, M.; Sun, H.; Li, G. R.; Fu, Q.; Li, H. B.; Liu, J.; Sun, L. Q.; Mauger, A.; Julien, C. M. et al. Constructing metal-free and cost-effective multifunctional separator for high-performance lithium-sulfur batteries. *Nano Energy* **2019**, *59*, 390–398.

[39] Dong, Q.; Shen, R. P.; Li, C. P.; Gan, R. Y.; Ma, X. T.; Wang, J. C.; Li, J.; Wei, Z. D. Construction of soft base tongs on separator to grasp polysulfides from shuttling in lithium-sulfur batteries. *Small* **2018**, *14*, 1804277.

[40] Cheng, Z. B.; Pan, H.; Chen, J. Q.; Meng, X. P.; Wang, R. H. Separator modified by cobalt-embedded carbon nanosheets enabling chemisorption and catalytic effects of polysulfides for high-energy-density lithium-sulfur batteries. *Adv. Energy Mater.* **2019**, *9*, 1901609.

[41] Kim, D. S.; Park, H. B.; Rhim, J. W.; Lee, Y. M. Preparation and characterization of crosslinked PVA/$SiO_2$ hybrid membranes containing sulfonic acid groups for direct methanol fuel cell applications. *J. Membr. Sci.* **2004**, *240*, 37–48.

[42] Zhu, Y. S.; Wang, X. J.; Hou, Y. Y.; Gao, X. W.; Liu, L. L.; Wu, Y. P.; Shimizu, M. A new single-ion polymer electrolyte based on polyvinyl alcohol for lithium ion batteries. *Electrochim. Acta* **2013**, *87*, 113–118.

[43] Jiang, K.; Gao, S.; Wang, R. X.; Jiang, M.; Han, J.; Gu, T. T.; Liu, M. Y.; Cheng, S. J.; Wang, K. L. Lithium sulfonate/carboxylate-anchored polyvinyl alcohol separators for lithium sulfur batteries. *ACS Appl. Mater. Interfaces* **2018**, *10*, 18310–18315.

[44] Liao, J. B.; Liu, Z.; Wang, J. L.; Ye, Z. B. Cost-effective water-soluble poly(vinyl alcohol) as a functional binder for high-sulfur-loading cathodes in lithium-sulfur batteries. *ACS Omega* **2020**, *5*, 8272–8282.

[45] Hays, K. A.; Ruther, R. E.; Kukay, A. J.; Cao, P. F.; Saito, T.; Wood III, D. L.; Li, J. L. What makes lithium substituted polyacrylic acid a better binder than polyacrylic acid for silicon-graphite composite anodes? *J. Power Sources* **2018**, *384*, 136–144.

[46] Li, N. W.; Shi, Y.; Yin, Y. X.; Zeng, X. X.; Li, J. Y.; Li, C. J.; Wan, L. J.; Wen, R.; Guo, Y. G. A flexible solid electrolyte interphase layer

for long-life lithium metal anodes. *Angew. Chem., Int. Ed.* **2018**, *57*, 1505–1509.

[47] Dai, J. H.; Shi, C.; Li, C.; Shen, X.; Peng, L. Q.; Wu, D. Z.; Sun, D. H.; Zhang, P.; Zhao, J. B. A rational design of separator with substantially enhanced thermal features for lithium-ion batteries by the polydopamine-ceramic composite modification of polyolefin membranes. *Energy Environ. Sci.* **2016**, *9*, 3252–3261.

[48] Xiao, W.; Zhang, K. Y.; Liu, J. G.; Yan, C. W. Preparation of poly(vinyl alcohol)-based separator with pore-forming additive for lithium-ion batteries. *J. Mater. Sci. Mater. Electron.* **2017**, *28*, 17516–17525.

[49] Cao, Y.; Liu, C.; Wang, M. D.; Yang, H.; Liu, S.; Wang, H. L.; Yang, Z. X.; Pan, F. S.; Jiang, Z. Y.; Sun, J. Lithiation of covalent organic framework nanosheets facilitating lithium-ion transport in lithium-sulfur batteries. *Energy Storage Mater.* **2020**, *29*, 207–215.

[50] Song, J. X.; Zhou, M. J.; Yi, R.; Xu, T.; Gordin, M. L.; Tang, D. H.; Yu, Z. X.; Regula, M.; Wang, D. H. Interpenetrated gel polymer binder for high-performance silicon anodes in lithium-ion batteries. *Adv. Funct. Mater.* **2014**, *24*, 5904–5910.

[51] Yang, Y. F.; Zhang, J. P. Highly stable lithium-sulfur batteries based on laponite nanosheet-coated celgard separators. *Adv. Energy Mater.* **2018**, *8*, 1801778.